Nucleation of dislocations and their dynamics in layered oxide cathode materials during battery charging

A. Singer[1,7], M. Zhang[2], S. Hy[2], D. Cela[1], C. Fang[2], T. A. Wynn[2], B. Qiu [ID][3], Y. Xia[3], Z. Liu[3], A. Ulvestad[4], N. Hua[1], J. Wingert[1], H. Liu[2], M. Sprung[5], A. V. Zozulya[5,8], E. Maxey[6], R. Harder[6], Y. S. Meng[2]* and O. G. Shpyrko[1]*

Lithium-rich layered oxides (LRLO) are among the leading candidates for the next-generation cathode material for energy storage, delivering 50% excess capacity over commercially used compounds. Despite excellent prospects, voltage fade has prevented effective use of the excess capacity, and a major challenge has been a lack of understanding of the mechanisms underpinning the voltage fade. Here, using operando three-dimensional Bragg coherent diffractive imaging, we directly observe the nucleation of a mobile dislocation network in LRLO nanoparticles. The dislocations form more readily in LRLO as compared with a classical layered oxide, suggesting a link between the defects and voltage fade. We show microscopically how the formation of partial dislocations contributes to the voltage fade. The insights allow us to design and demonstrate an effective method to recover the original high-voltage functionality. Our findings reveal that the voltage fade in LRLO is reversible and call for new paradigms for improved design of oxygen-redox active materials.

The lithium-rich layered oxide (LRLO) compounds are among the most promising positive electrode materials for next-generation batteries. They exhibit high capacities of $>300\,\mathrm{mAh\,g^{-1}}$ due to the unconventional participation of the oxygen anion redox in the charge compensation mechanism[1–8], suggested by the localization of $2p$ O electrons[5,6,8,9] or by the formation of Li_2O (ref. [10]) or of O–O peroxide dimers during operation[11]. The LRLO material is a composite of a classical layered oxide $LiTMO_2$ (with $R\overline{3}m$ space group, where TM stands for Ni, Mn, Co) and Li_2TMO_3 (with $C2/m$ space group). In some systems, the excess capacity results from the activation of inactive monoclinic Li_2TMO_3 into active layered material[12].

The local composition of cations and their associated interaction is crucial for lithium diffusion capabilities and voltage stability[3,13,14]. Two prevailing theories for the notorious voltage fade are the surface phase transformation from layered to defect spinel[9] with a layer of a few nanometres (ref. [15]) and the irreversible migration of transition-metal ions into octahedral sites in the lithium layer or interstitial vacant tetrahedral sites[3]. Nevertheless, the theories appear incomplete as the voltage recovery prevents exploiting the full potential of the LRLO materials.

The capacity fade, a second major challenge in LRLO, has been resolved[16]. X-ray and neutron scattering measurements revealed that the layer spacing (c lattice parameter) expands during charge from 14.25 Å to about 14.40 Å with simultaneous contraction of the ab plane[17], resulting in significant volume changes and cracking of secondary particles on the initial charge to 4.5 V (ref. [18]). Indeed, the formation of cracks and stress-induced damage in secondary particles has been identified in other layered oxides and is believed to be a leading cause of degradation and debilitating electrochemical

performance[19–21]. The large secondary particles (tens of micrometres in size) are agglomerates of much smaller (sub-micrometre) single-crystalline primary particles, and such morphologies are introduced to improve the volumetric energy density of the cathode (see Supplementary Fig. 1).

Despite their fundamental importance, the understanding of structural evolution during charge in the primary particles remains challenging. Particularly the nature of crystal defects, which are expected to occur with Burgers vectors parallel to the layers during operation[19,22], remains elusive due to the difficulty in capturing their operando formation and dynamics[23–25].

Here, we directly capture the nucleation of a dislocation network in primary nanoparticles of the high-capacity LRLO material $Li_{1.2}Ni_{0.133}Mn_{0.533}Co_{0.133}O_2$ during electrochemical charge (lithium extraction) (see Fig. 1). Based on the discovery of defect formation and first-principles calculations, we identify the origin of the voltage fade, allowing us to design and experimentally demonstrate a treatment to restore the voltage in LRLO.

Operando 3D imaging of the dislocation nucleation

By using the in situ Bragg coherent diffractive imaging (BCDI) technique[24,26–28], we map the 3D displacement field inside primary battery particles during battery operation (see Methods and Supplementary Figs. 2 and 3). Dislocations give rise to singularities in the displacement field, which are easily recognizable even in the presence of noise[29]. We find that while the pristine nanoparticle shows no such singularities in the present geometry (see Fig. 1a and Supplementary Video 1), when charged to a voltage of 4.3 V versus (vs) Li+ it contains two dislocations in the bulk of the

[1]Department of Physics, University of California-San Diego, La Jolla, California, USA. [2]Department of NanoEngineering, University of California-San Diego, La Jolla, California, USA. [3]Ningbo Institute of Materials Technology and Engineering (NIMTE), Chinese Academy of Sciences, Zhejiang, China. [4]Materials Science Division, Argonne National Laboratory, Argonne, Illinois, USA. [5]Deutsches Elektronen-Synchrotron DESY, Hamburg, Germany. [6]X-ray Science Division, Advanced Photon Source, Argonne, Illinois, USA. [7]Present address: Cornell University, Ithaca, New York, USA. [8]Present address: European XFEL GmbH, Schenefeld, Germany. *e-mail: shirleymeng@ucsd.edu; oshpyrko@physics.ucsd.edu
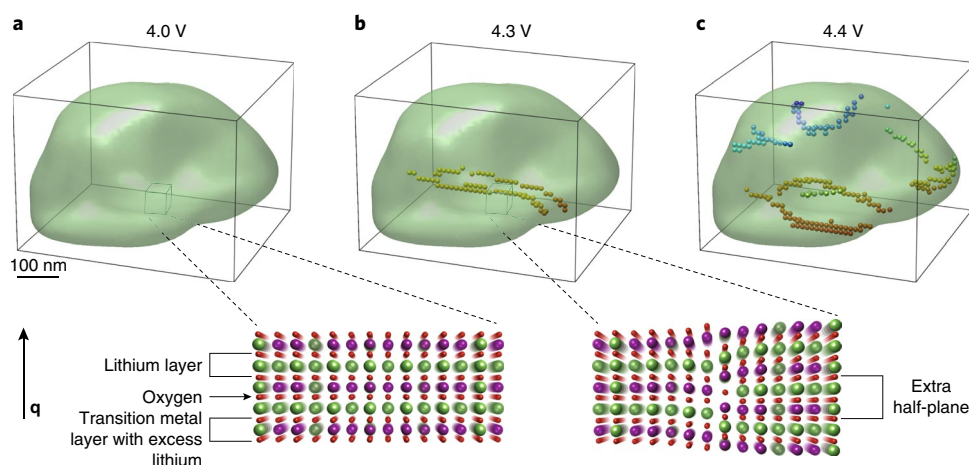
Fig. 1 | Formation of a dislocation network during charge. Isosurface rendering of a LRLO particle measured in operando during charge. **a**, At a charge state of 4.0 V versus Li+ no dislocations are observed in the particle. The inset shows a schematic of a dislocation-free crystal. **b**, At 4.3 V two edge dislocations have formed during lithium extraction (shown by small spheres in the particle). The inset shows a schematic of an edge dislocation. **c**, At 4.4 V a dislocation network emerges (colours are used to represent different dislocations). The direction of the X-ray scattering vector **q** (perpendicular to the layers) is indicated and the size of the particle is around $300 \times 300 \times 500 \, nm^3$.
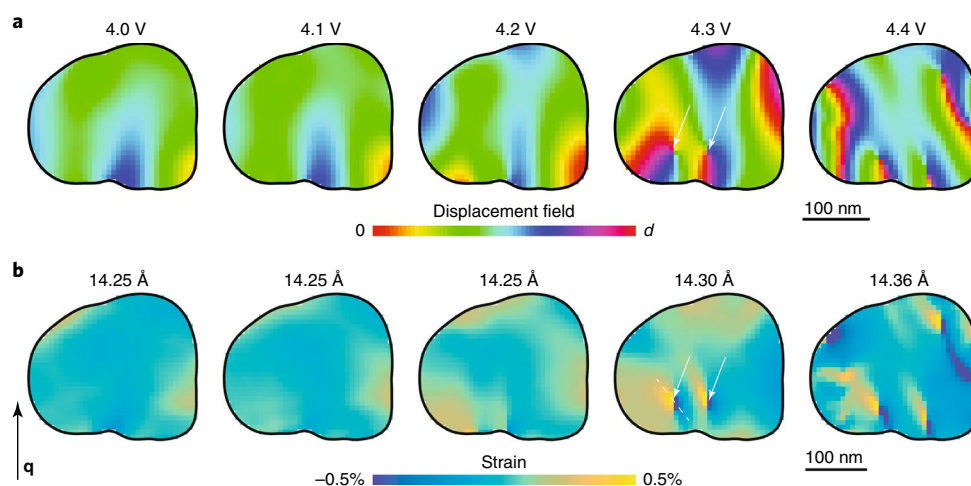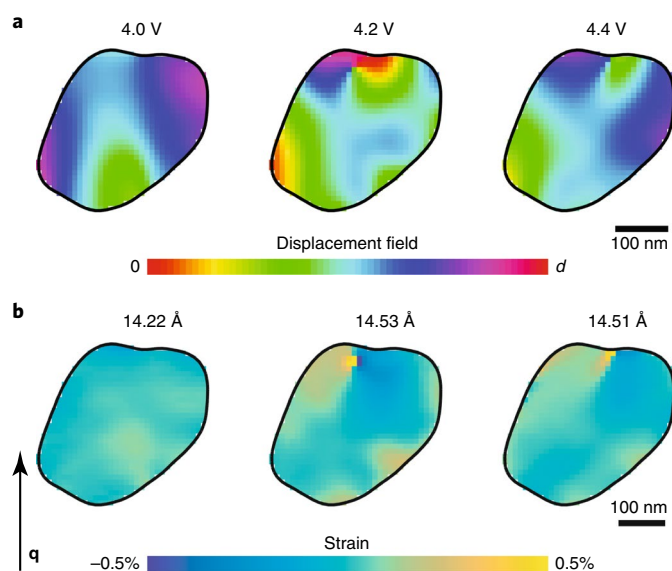

Fig. 2 | In situ evolution of a LRLO nanoparticle during electrochemical charge. a, The changes in the displacement field along **q** in a plane through the nanoparticle during charge (the plane is shown in Supplementary Fig. 2). The voltage versus Li+ is indicated at the top. Two edge dislocations are identified as singularities of the displacement field and are indicated at 4.3 V vs Li+ (see Fig. 1b). Additional dislocations emerge at 4.4 V vs Li+. **b**, The strain along the (001) direction (perpendicular to the layers) inside of the nanoparticle calculated from the 3D displacement fields in **a**. The strain is shown around the average lattice constant indicated at the top. White arrows indicate the positions of the edge dislocations at 4.3 V vs Li+.

nanoparticle (see Fig. 1b and Supplementary Video 2), revealing the formation of dislocations in bulk during charge. The dislocation density increases on subsequent charge, and a dislocation network emerges at 4.4 V vs Li+ (see Fig. 1c). We identify the crystal imperfections as line defects with the Burgers vector having a component along the *c*-axis direction, perpendicular to the layers, resembling Frank partial dislocations[30].

The in situ BCDI technique allows us to directly image the interior of a nanoparticle during lithium extraction (battery charge) operando (see Fig. 2). In the beginning of the charge at 4.0 V, we observe a continuous displacement field. At 4.2 V the displacement field has changed only slightly, an expected structural response of the nanoparticle to delithiation[17]. When charged to 4.3 V, immediately before the voltage plateau that signifies oxygen evolution[10], the displacement field is qualitatively different and shows two singularities characteristic of dislocations. The discontinuity in

the displacement field around a singularity is the projection of the Burgers vector along the scattering vector **q**, which matches the thickness of a single TM or lithium layer (see Fig. 1 for a schematic). Further charging to 4.4 V vs Li+ induces additional dislocations, while the two edge dislocations present at 4.3 V move slightly. By analysing the dislocation type in various particles during lithium extraction, we find the presence of edge, screw and mixed dislocations. We are unable to perform reliable BCDI at voltages higher than 4.4 V, possibly due to growing disorder in the structure; however, further broadening of the Bragg diffraction suggests continued formation of dislocations (see Supplementary Figs. 4 and 5).

The strain field distribution yields further insights into the physical and electrochemical processes underpinning the formation of dislocations (see Fig. 2b). The strain inhomogeneity in the slice shown increases between 4.0 V and 4.2 V and the strain is larger towards the bottom left edge of the particle, suggesting elevated

a

4.0 V   4.2 V   4.4 V

Displacement field

100 nm

0   d

b

14.22 Å   14.53 Å   14.51 Å

100 nm

q

Strain

−0.5%   0.5%

Fig. 3 | In situ evolution of a NCA nanoparticle during charge.
a,**b**, Displacement field (**a**) and strain (**b**) along the (001) direction (perpendicular to the layers) of a single NCA particle captured in situ during charge. The voltages and average lattice constants are indicated.

delithiation. At 4.3 V a plastic deformation occurs via nucleation of two dislocations in the bulk. Around these dislocations, the strain is compressive (reduced lattice spacing d) on the right and tensile on the left, revealing extra half-planes on the right in agreement with the displacement field analysis (see schematic in Fig. 1). Modelling of strain profiles indicates that most of the dislocations are mixed c and a–b dislocations (see Methods and Supplementary Fig. 6). We have conducted measurements on two different nanoparticles, and both of them show the formation of multiple dislocations during charge (see Supplementary Fig. 7).
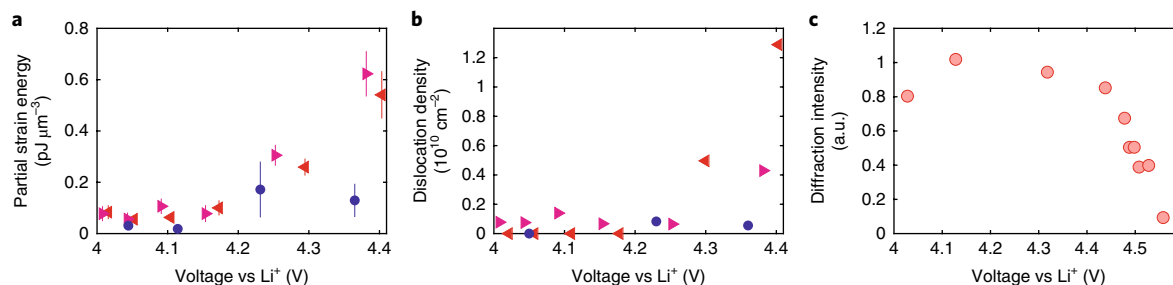
To have a direct comparison between LRLO and currently commercialized layered oxides, we have conducted operando BCDI on a classical layered oxide material ($LiNi_{0.80}Co_{0.15}Al_{0.05}O_2$, 'NCA') (see Fig. 3). Strikingly, though we find that dislocations form in the classical material as well, their number is significantly less than in LRLO (in a different NCA nanoparticle no dislocations formed during delithiation to 4.8 V). In the nanoparticle of the classical material a single dislocation forms at 4.2 V; however, no new dislocations appear above 4.2 V. We calculate the partial strain energy in the (001) direction via $E_{p,001} = \frac{1}{2} Y \int \varepsilon_{001}(x)^2 dx$, where Y is Young's

modulus[31], $\varepsilon_{001}(x)$ is the measured strain shown in Figs. 2b and 3b, x is the spatial coordinate, and we integrate over the particle volume. The strain energy for LRLO materials grows monotonically up to 4.4 V, whereas it peaks at 4.2 V for NCA and reduces on further lithium extraction. The strain calculations shown in Fig. 4a are in excellent agreement with the Williamson–Hall analysis of synchrotron powder diffraction data, which shows a gradual increase in the microstrain during charge from 4.0 V to 4.7 V for LRLO and a peak at 4.3 V for NCA (see Supplementary Fig. 5). The agreement between the strain measurements in single nanoparticles in operando BCDI and bulk powder diffraction data confirms that the particles shown in Figs. 2 and 3 are representative of the ensembles. In LRLO, the microstrain continues growing above 4.4 V, the range inaccessible in BCDI, thus suggesting further dislocation formation at high voltages between 4.4 V and 4.7 V.

In LRLO, the lithium ion diffusion drops from $D = 10^{-14}\,cm^2\,s^{-1}$ at 4.0 V below $D = 10^{-15}\,cm^2\,s^{-1}$ at 4.4 V (ref. [32]). Using Fick's law $\langle x^2 \rangle = 4D\tau$, where τ is the diffusion time, we determine an average travel distance of lithium ions to be $\sqrt{\langle x^2 \rangle} \sim 40\,nm$ in one hour, which is an order of magnitude smaller than the size of the nanoparticles. Lithium extraction during charge coupled with slow diffusion will result in lithium-depleted regions at the particle boundary. Thus, we argue that in LRLO the dislocations possibly form as a result of strain concentrators due to the volume difference between regions with low and high lithium concentrations. In the classical layered oxide materials, the diffusion rate is higher and the ductility is lower[33], which results in the dramatic difference between the rates of dislocation formation in the LRLO and classical layered materials. By tracking the location of two dislocations that formed at 4.3 V in LRLO (see arrows in Fig. 2), we estimate the speed of dislocations to be on the order of 10 nm h⁻¹. This speed is comparable with lithium mobility, indicating ionic diffusion as the dominant reason for dislocation motion. A different hypothesis for dislocation formation is the transition metal migration facilitated by oxygen redox activity[34]: lithium, transition metal, and oxygen vacancies may result in localized vacancy loops[30], which develop into the observed edge dislocations extending over the whole nanoparticle.

Dislocation network as the origin of the voltage fade

By measuring the length of dislocations in single nanoparticles, we directly calculate the dislocation density to be $10^{10}\,cm^{-2}$ in LRLO at 4.4 V (note that in NCA the density is approximately one order of magnitude smaller, see Fig. 4b). At such a high value, we anticipate a sizable impact on the material's performance, particularly on voltage fade and oxygen activity. Though the strain energy is negligible compared to the total capacity of the fully charged material, the nucleation of line defects dramatically modifies the local lithium

a

Partial strain energy ($pJ\,\mu m^{-3}$)

Voltage vs Li⁺ (V)

b

Dislocation density ($10^{10}\,cm^{-2}$)

Voltage vs Li⁺ (V)

c

Diffraction intensity (a.u.)

Voltage vs Li⁺ (V)

Fig. 4 | Strain energy landscape of single particles of layered oxides. a, Partial strain energy $E_{p,001}$ for two LRLO particles shown in Figs. 1, 2 (red triangles) and Supplementary Fig. 7 (magenta triangles), and a NCA particle shown in Fig. 3 (blue circles). **b**, Operando evolution of the dislocation density ρ_0 for the same particles. **c**, Evolution of the superstructure diffraction peak intensity (see Supplementary Fig. 13) during the first charge measured in situ using X-ray diffraction from a large number of particles. The uncertainties in **a** represent the standard deviation between strains calculated using various thresholds for the reconstructed amplitude in phase retrieval (10 equidistantly spaced values between 0.1 and 0.2).
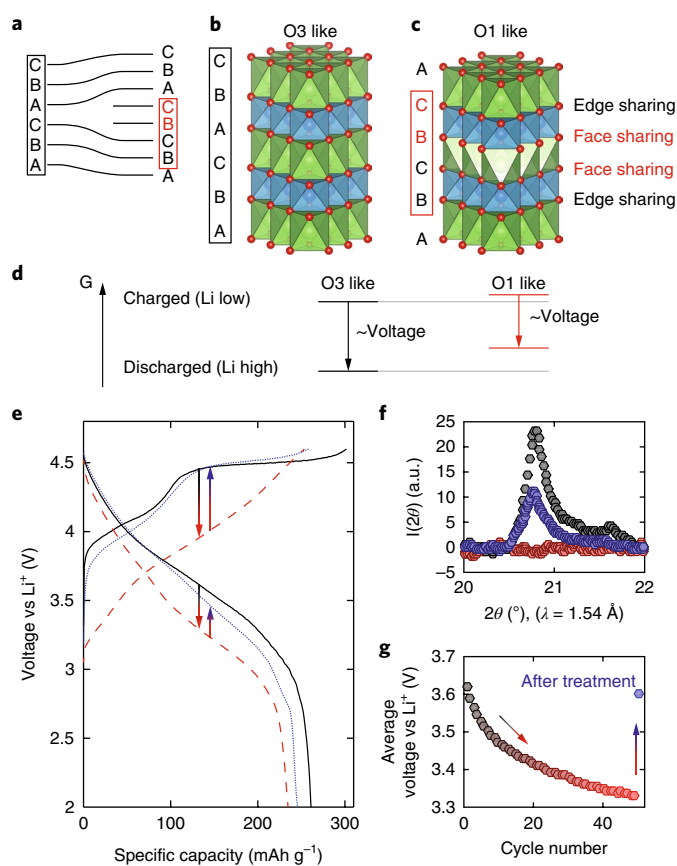
Fig. 5 | A path to restore the voltage in the lithium-rich oxide material.
a–c, Schematic of the oxygen layers stacking modification induced by a partial dislocation (**a**): two extra oxygen layers break up the O3 sequence ABCABC (**b**) into a O1 like sequence ABC BC ABC (**c**) or ABC AB ABC or ABC AC ABC (not shown). Dislocation formation results in a mixture between O3 and O1 sequences. Edge sharing between the Li and TM octahedral sites occurs in O3, while face sharing occurs in O1. **d**, In the phenomenological Gibbs free energy diagram, edge-sharing octahedra result in the energetically most favourable configuration. The face-sharing configuration raises the energy, particularly for high lithium concentrations. First-principles calculations yield a voltage of 4.6 V (O3 like) and 4.1 V (O1 like) in the fully discharged state (see Supplementary Figs. 14 and 15). **e**, Charge–discharge voltage curves of Li-rich layered cathode with Li-metal as anode for the voltage range of 2.0–4.6 V vs Li$^+$/Li: the first cycle (black solid lines), 50th cycle (red dashed lines), and the cycle after heat treatment (blue dotted lines) are shown (the sequence of measurements is indicated by arrows). **f**, The evolution of the superstructure peak intensity in the pristine state (black symbols), after 50 cycles (red symbols), and after the heat treatment (blue symbols). **g**, The average discharge voltage for the first 50 cycles (black to red symbols) and after the heat treatment (blue symbol) measured in a 2032-type half-cell. The discharge voltage is recovered after the treatment.

environment by perturbing the sequence of oxygen layers (see Fig. 5a). The extra half-plane contains two oxygen layers (see Fig. 1); thus, the initial sequence ABCABC (O3 in the notation introduced by Delmas et al.[35]) transforms to ABC BC ABC (see Fig. 5a), which contains an O1-like part BCBC. In the energetically most favourable O3 structure, all lithium octahedral sites share edges with transition metal octahedral sites (see Fig. 5b). The partial transition to O1 induces unfavourable face sharing between lithium and transition metal octahedral sites (see Fig. 5c), thus raising the Gibbs free energy of the system (see Fig. 5d). This energy penalty is greater

at high lithium concentration simply because more face-sharing sites are filled (see Fig. 5d and first-principles calculations in the Methods and Supplementary Figs. 14 and 15). We postulate that the difference in free energy induced by the presence of O1-like defects contributes to the voltage fade. The excess lithium stabilizes the coexistence of O3- and O1-like structures around a single dislocation by lowering the energy difference between O3 and O1: the face-sharing energy penalty of Li–Li sites is smaller than that of Li–TM sites.

Voltage recovery

We directly confirm the perturbation of the stacking sequence of the layers through the decline of the superstructure peak in in situ X-ray diffraction starting at 4.3 V (see Fig. 4c). Even if the dislocation disappears by moving out of the particle or by annihilation with other dislocations, the superstructure is unlikely to recover once a dislocation has formed. The dislocation formation due to strain observed in single-particle imaging experiments up to 4.4 V, and continued growth of strain from in situ powder microstrain measurements up to 4.7 V, suggest the dislocations continue to form up to 4.7 V, consistent with superstructure fade up to 4.7 V. During the subsequent cycling, the superstructure gradually disappears (see Supplementary Fig. 13), and the material becomes partially disordered. The highly cycled material is trapped in a metastable state with an energetically unfavourable local lithium environment. Based on the mechanistic description above we design a path to re-order the superstructure by high-temperature annealing (>150 °C). The voltage profile after treatment (see Fig. 5e) shows recovery of the voltage and activation during charge, associated with oxygen redox activity and potentially oxygen release[6]. The treatment at high temperatures recovers the superstructure (see Fig. 5f) and presumably the oxygen stacking sequence, which is decisive in restoring the original voltage profile (see Fig. 5g).

Discussion

The experimental observation of a significantly higher rate of dislocation formation in LRLO as compared with classical material resonates with the excess capacity in LRLO. As our X-ray data show no evidence of a two-phase composite, we rule out excess capacity due to the activation of monoclinic L$_2$MnO$_3$ at high voltages. The current understanding of the anionic activity in LRLO materials includes three processes: step 1—reversible oxidation of O^{2-} to O$^-$; step 2—further partially reversible oxidation to O; and step 3—irreversible release of O$_2$ gas from the bulk material to the surface[7]. Steps 2 and 3 require elevated oxygen mobility in the bulk. While enhanced 'pipe' diffusion occurs along dislocations[36], recent theoretical works suggest a slower transport of oxygen along dislocations due to cation charge accumulation at the defect site[37]; oxygen mobility due to thermal fluctuations is predicted to be negligible at room temperature. However, an external electrical current leads to reversible accumulation or depletion of oxygen vacancies at dislocations in SrTiO$_3$ (ref. [38]); dislocations play a major role in redox-based resistive switching in transition metal oxides used for memristive applications[39]. Similarly, we posit that during charge the lithium and electron extraction activates the emergent dislocation network in LRLO for the transport of oxygen vacancies. The oxygen vacancy mobility is probably accommodated by undesired side effects such as cation disorder and stacking faults, which debilitate oxygen redox activity[5]. The recovery of the voltage plateau after the heat treatment indicates the elimination of structural disorder and restoring of the cation ordering. We cannot exclude the contribution of surface effects to the reappearance of the voltage plateau[8]. A combination of spectroscopic and imaging techniques is required to better quantify the connection between oxygen activity and defects in the future.

Methods

Experimental details. The design of the in situ cells is described elsewhere[24,40]. The batteries were mounted on sample holders manufactured using a 3D printer (see Supplementary Fig. 2). The electrode was prepared with 80% of active material, 10% binder and 10% carbon black. The cells were charged to 4.1 V and discharged to 3.5 V three times, which improved the stability and electrochemical response of the nanoparticles. Charging to these low voltages is completely reversible. The experiments on LRLO were conducted at the 34 ID beamline of the Advanced Photon Source (Argonne National Laboratory, ANL, USA). A photon energy of 9 keV and a sample-to-detector distance of 60 cm were used in the experiments. The experiments on NCA were conducted at the P10 beamline of PETRA III (Deutsches Elektronen Synchrotron, DESY, Germany) with a photon energy of 9.6 keV and a sample-to-detector distance of 182 cm. Timepix (34ID) or Lambda (P10) 2D detectors were used, both with a pixel size of 55 μm × 55 μm. Supplementary Fig. 3 shows the electrochemical profiles measured simultaneously with the X-ray data on the in-situ cell. Supplementary Figs. 4, 8 and 9 show slices through typical X-ray diffraction profiles.

X-ray data collection and reconstruction procedure. In all experiments rocking scans, approximately 1° wide with 30–60 points, were collected. During the analysis, various reconstruction procedures were tested, including combinations of error-reduction (ER) alternating with hybrid input-output (HIO), relaxed averaged alternating reflections (RAAR) or difference map (DM) algorithms[41,42]. The diffraction data was cropped (APS data) or binned (PETRA III data) to 128× 128 pixels before running reconstructions. The number of iterations was varied between 410 and 2,000. All attempts resulted in very similar reconstructions. In this work we used an average of 10 results, each being an average of 25 reconstructions retrieved in a guided procedure developed in ref.[27] (5 generations, 50 population). The shape of the nanoparticle was found by averaging the amplitudes of the reconstructions at different voltages, assuming the nanoparticle shape change during charge is negligible, and applying a threshold to that average amplitude. The individual amplitudes of the nanoparticle at different voltages are indeed very similar, except for the regions in the vicinity of forming dislocations, where the amplitude goes to zero. The reconstructions were run using a GPU-optimized code on multiple GeForce Titan Black graphics cards.

Identifying the defect network. The dislocations were identified using the method presented in ref.[27]. The dislocation density was calculated by dividing the integrated dislocation length of the network by the volume of the nanoparticle. Though the resolution defined by the phase retrieval transfer function is about 100 nm, the positions of the dislocations are resolved to a much higher precision (see Supplementary Figs. 10 and 11), possibly because the core of the dislocation is determined by the long-range displacement field.

Model calculations within the isotropic elastic model. The displacement and strain fields around dislocations provide unique access to the local elastic properties of the material as well as the exact nature of the dislocations[24,30]. We have used the isotropic model to calculate the displacement field around an edge dislocation[30]

$$u_x = \frac{b}{2\pi}\left[tan^{-1}\left(\frac{y}{x}\right) + \frac{xy}{2(1-\nu)(x^2+y^2)} \right] \tag{1}$$

$$u_y = -\frac{b}{2\pi}\left[\frac{1-2\nu}{4(1-n\nu)}log(x^2+y^2) + \frac{x^2-y^2}{4(1-\nu)(x^2+y^2)} \right] \tag{2}$$

where u_x and u_y are the displacements perpendicular and parallel to the extra plane, respectively, b is the modulus of the Burgers vector and ν is the Poisson ratio (assumed 0.3 here[31]). The strain was calculated using equations (1, 2) as the derivative of the displacement field along the $\mathbf{q}$ vector, $u_{\mathbf{q}}$. For a Burgers vector parallel to $\mathbf{q}$, $u_{\mathbf{q}} = u_x$, and the resulting displacement and strain are shown in Supplementary Fig. 6a–c, which is in reasonable agreement with the measurements in NCA (see Supplementary Fig. 6d). The displacement and strain field in LRLO is not well reproduced with this model calculation (see Supplementary Fig. 6h), and we identify the {403} planes (see Supplementary Fig. 6i) as likely candidates to form the half plane dislocations, as in this plane oxygen vacancies are more likely to develop[16]. This plane has an angle of 52° with respect to the layers. Supplementary Fig. 6e–h shows the corresponding displacement field, which agrees qualitatively with the measurements in LRLO.

Microstrain and superstructure analysis. The microstrain was analysed by examining the line broadening observed in the synchrotron X-ray diffraction (SXRD) patterns, which were collected at the Advanced Photon Source at the Argonne National Laboratory. The wavelength of the X-ray source is 0.11165 Å for LRLO and 0.414215 Å for NCA samples. The data for LRLO was measured in situ, while NCA was measured ex situ. Williamson−Hall analysis of all peaks that exhibit the best linear fitting was carried out for a quantification of microstrain

changes during the initial charging process[43]. The instrumental broadening was corrected based on the standard sample CeO_2 using the following equation:

$$FW(S)^D = FWHM^D - FW(I)^D \tag{3}$$

where FWHM is measured full-width at half-maximum of each peak; FW(S) and FW(I) are the calculated full-widths for the sample and instrument, respectively; D is the deconvolution parameter, which is set to be 1.5 for all the analysis. The sample peak broadening is ascribed to particle size and microstrain based on the Williamson–Hall method by the following equation:

$$FW(S)\ cos(\theta) = \frac{K\lambda}{Size} + 4 \times Strain \times sin(\theta) \tag{4}$$

where K is the crystallite shape factor (assumed to be 0.9), θ is the diffraction angle and λ is the X-ray wavelength of the source. The microstrain is extracted from the slope of the plot of FW(S) cos(θ) versus 4 sin(θ). For the LRLO sample, the microstrain gradually increases until 4.5 V and keeps increasing even more rapidly after 4.5 V (see Supplementary Fig. 5a). The maximum microstrain for the NCA sample occurs around 4.3 V and the microstrain reduces on further charging (see Supplementary Fig. 5b). The superstructure peak was analysed in the data used for the Williamson–Hall analysis. The superstructure peak height was determined as the peak intensity after background subtraction and normalization (see right inset in Fig. 4).

Absence of surface effects in the voltage fading process. The voltage fade mechanism presented in the main text is a bulk effect. To exclude the contribution of surface effects in the voltage fade mechanism we measured the average charge and discharge voltage during cycling for the initial 50 cycles (see Supplementary Fig. 12). When the surface impedance development dominates the voltage fading process, the average charge voltage increases during the cycling to compensate the IR drop. However, both charge and discharge average voltage of LRLO material decrease during the extended cycles (see Supplementary Fig. 12), which shows that bulk effects dominate the voltage fade in the material investigated in this manuscript.

Computational methods. The influence of the oxygen stacking sequence on the voltage decay in LRLO material was investigated by first-principles calculations. For simplicity, a supercell model composed of three-formula units of $Li_{12}Mn_6O_{18}$ was used for the LRLO structure with different oxygen stacking sequence O3 and O1. A specific lithium concentration range $Li_{12-x}Mn_6O_{18}$ ($0 \leq x \leq 4$) was chosen to simulate the initial stage of charge, corresponding to the delithiation range in the BCDI measurement. Calculations were performed in the spin-polarized GGA + U approximations to the density functional theory (DFT). The core-electron states were represented by the projector-augmented-wave method[44] as implemented in the Vienna ab initio simulation package[45]. We used the Perdew–Burke–Ernzerhof exchange correlation, and a plane-wave representation for the wavefunction with a cutoff energy of 450 eV (ref.[46]). The Brillouin zone was sampled with a dense k-points mesh by Gamma packing. To obtain the Gibbs free energy and optimized cell structure, the atomic positions and cell parameters were fully relaxed. The Gibbs free energy for each delithiation composition of the supercell was determined by analysing the energies of all permutations of lithium removal. The Gibbs free energy for the O3 stacking is lower than for the O1 stacking for all delithiation compositions (see Table 1 and Supplementary Fig. 14), confirming O3 stacking is the stable structure without face-sharing sites between Li and TM octahedra. To obtain the formulas of stable phases, the formation energy (see Supplementary Fig. 15a) of $Li_{12-x}Mn_6O_{18}$ ($0 \leq x \leq 4$) versus lithium concentration was calculated with two reference states set, as $x = 0$ and $x = 4$, by:

$$E_{Li_{12-x}Mn_6O_{18}} = G_{Li_{12-x}Mn_6O_{18}} - [(4-x)/4] \times G_{Li_{12}Mn_6O_{18}} - (x/4) \times G_{Li_8Mn_6O_{18}} \tag{5}$$

where E_i and G_i are the formation energy and Gibbs free energy of that particular lithium concentration. The tie lines that connect all the lowest formation energies with different lithium concentration allow one to determine the phase stability. When the formation energy of a particular lithium concentration is above the tie line, it is unstable with respect to a mixture of the two phases with the lithium concentration that defines the end points of the tie line. The cathode chemical potential for a stable structure can be approximated by:

$$\mu_{Li}^{Li_{12-x}Mn_6O_{18}} = \frac{dG_{Li_{12-x}Mn_6O_{18}}}{dN_{Li}} \approx G_{Li_{(12-x)+1}Mn_6O_{18}} - G_{Li_{12-x}Mn_6O_{18}} \tag{6}$$

where μ_i is the chemical potential of element i and N_i is the amount of element i. The cathode chemical potential for a lithium concentration with an unstable structure is equal to the first derivative of the Gibbs free energy with respect to the lithium amount for the end points of the tie-line only. From the cathode chemical potential, the voltage (see Supplementary Fig. 15b) for stacking sequence O3 and O1 was obtained from the Nernst equation:

$$\text{Voltage(vs Li/Li}^+) = \frac{\mu_{Li}^{anode} - \mu_{Li}^{cathode}}{n_e} = \frac{-1.9\,eV - \mu_{Li}^{Li_{12-x}Mn_6O_{18}}}{e} \quad (7)$$

where $\mu_{Li}^{cathode}$ is the chemical potential per atom of Li in the cathode, μ_{Li}^{anode} is the chemical potential per atom of Li in the anode (and equals $-1.9\,eV$), and n_e is the number of transferred electrons per lithium atom. The calculated voltage for the LRLO supercell with O3 stacking matches well with the experimental measurements of the first cycle charging voltage[47]. O3 shows a higher average voltage relative to the O1 phase at least through a lithium concentration of 8/12, suggesting the formation of stacking faults is one source of the voltage fade in LRLO cathodes.

Note, that the slope of the Gibbs free energy as a function of lithium concentration is a rough estimate for the average voltage, provided all concentrations are stable. Because we anticipate the Gibbs free energies for O3 and O1 to be similar when all lithium is extracted ($x = 12$), the average slope of the O3 curve is steeper, resulting in a higher average voltage (see Supplementary Fig. 14).

High-temperature annealing of cycled LRLO electrode. To evaluate the electrochemical performance of cycled LRLO material after high-temperature annealing, 18650-type cylindrical Li-ion batteries were assembled with LRLO as the cathode, spinel $Li_4Ti_5O_{12}$ (LTO) as the anode, and polyethylene as the separator. A direct annealing of the electrodes cycled in 2032-type cells resulted in the detachment of the electrode from the current collector, preventing us from electrochemically testing the annealed material. The little amount of the active material in a coin cell electrode (6 mg) is insufficient to prepare new electrodes. By using an 18650-type battery, we were able to electrochemically cycle a large amount of the cathode material, allowing the preparation of electrodes for cycled and annealed cathode materials. For electrochemical cycling in the 18650-type battery we selected LTO as the anode due to its slightly better cycling performance as compared with lithium metal.

The positive electrode consisted of 94.5 wt.% LRLO, 3.0 wt.% conductive graphite and 2.5 wt.% poly-vinylidene fluoride (PVDF). The loading amount of the cathode material on each side of the positive electrode was about 10 mg cm^{-2}. The negative electrode consisted of 90.5 wt.% LTO, 5.0 wt.% conductive graphite and 4.5 wt.% PVDF. The loading amount of the anode material on each side of the negative electrode was about 16 mg cm^{-2}. After the formation cycle, the batteries were directly cycled in the voltage range from 1.0 V to 3.25 V vs LTO at 0.1 C-rate at room temperature.

The fully discharged batteries after the 50th cycle were dissembled in the argon-filled glove box. LRLO cathodes were rinsed several times with dimethyl carbonate (DMC) and, once dry, scraped off from the current collector, and finally annealed in the box furnace at a temperature greater than 150 °C for one hour under an Ar atmosphere. After heat treatment, the LRLO cathodes were dissolved in N-methyl pyrrolidone (NMP) to form slurries that were cast on Al-foil and dried under vacuum at 80 °C for 12 h. The electrode discs were punched and used as the cathode to assemble coin cells (2032-type) with metallic Li as the counter electrode to assess the impact of heat treatment on the average discharge voltage. Because our measurements concentrate on the cathode material, we do not expect the difference in the testing battery systems to be significant; the voltage recovery reflects the real structural transformations after heat treatment.

Data availability. The data that support the plots within this paper and other findings of this study are available from the corresponding authors upon reasonable request. The X-ray imaging data are deposited at Sector 34-ID-C of the Advanced Photon Source and Sector P10 at the Petra-III source.

References

1. Lee, J. et al. Unlocking the potential of cation-disordered oxides for rechargeable lithium batteries. *Science* **343**, 519–522 (2014).
2. Sathiya, M. et al. Reversible anionic redox chemistry in high-capacity layered-oxide electrodes. *Nat. Mater.* **12**, 827–835 (2013).
3. Sathiya, M. et al. Origin of voltage decay in high-capacity layered oxide electrodes. *Nat. Mater.* **14**, 230–238 (2015).
4. Nitta, N., Wu, F., Lee, J. T. & Yushin, G. Li-ion battery materials: present and future. *Mater. Today* **18**, 252–264 (2015).
5. Seo, D.-H. et al. The structural and chemical origin of the oxygen redox activity in layered and cation-disordered Li-excess cathode materials. *Nat. Chem.* **8**, 692–697 (2016).
6. Luo, K. et al. Charge-compensation in 3d-transition-metal-oxide intercalation cathodes through the generation of localized electron holes on oxygen. *Nat. Chem.* **8**, 684–691 (2016).
7. Delmas, C. Battery materials: Operating through oxygen. *Nat. Chem.* **8**, 641–643 (2016).
8. Renfrew, S. E. & McCloskey, B. D. Residual lithium carbonate predominantly accounts for first cycle CO$_2$ and CO outgassing of Li-stoichiometric and Li-rich layered transition-metal oxides. *J. Am. Chem. Soc.* **139**, 17853–17860 (2017).
9. Xu, B., Fell, C. R., Chi, M. & Meng, Y. S. Identifying surface structural changes in layered Li-excess nickel manganese oxides in high voltage lithium ion batteries: A joint experimental and theoretical study. *Energy Environ. Sci.* **4**, 2223 (2011).
10. Hy, S., Felix, F., Rick, J., Su, W.-N. & Hwang, B. J. Direct in situ observation of Li$_2$O evolution on Li-rich high-capacity cathode material, Li[Ni$_x$Li$_{(1-2x)/3}$Mn$_{(2-x)/3}$]O$_2$ ($0 \leq x \leq 0.5$). *J. Am. Chem. Soc.* **136**, 999–1007 (2014).
11. McCalla, E. et al. Visualization of O–O peroxo-like dimers in high-capacity layered oxides for Li-ion batteries. *Science* **350**, 1516–1521 (2015).
12. Ye, D. et al. Understanding the origin of Li$_2$MnO$_3$ activation in Li-rich cathode materials for lithium-ion batteries. *Adv. Funct. Mater.* **25**, 7488–7496 (2015).
13. Seymour, I. D. et al. Characterizing oxygen local environments in paramagnetic battery materials via ^{17}O NMR and DFT calculations. *J. Am. Chem. Soc.* **138**, 9405–9408 (2016).
14. Croy, J. R., Balasubramanian, M., Gallagher, K. G. & Burrell, A. K. Review of the U.S. Department of Energy's 'Deep Dive' effort to understand voltage fade in Li- and Mn-rich cathodes. *Acc. Chem. Res.* **48**, 2813–2821 (2015).
15. Boulineau, A., Simonin, L., Colin, J.-F., Bourbon, C. & Patoux, S. First evidence of manganese–nickel segregation and densification upon cycling in Li-rich layered oxides for lithium batteries. *Nano Lett.* **13**, 3857–3863 (2013).
16. Qiu, B. et al. Gas–solid interfacial modification of oxygen activity in layered oxide cathodes for lithium-ion batteries. *Nat. Commun.* **7**, 12108 (2016).
17. Liu, H. et al. Operando lithium dynamics in the Li-rich layered oxide cathode material via neutron diffraction. *Adv. Energy Mater.* **6**, 1502143 (2016).
18. Chen, C.-J. et al. The origin of capacity fade in the Li$_2$MnO$_3$·LiMO$_2$ (M = Li, Ni, Co, Mn) microsphere positive electrode: An operando neutron diffraction and transmission X-ray microscopy study. *J. Am. Chem. Soc.* **138**, 8824–8833 (2016).
19. Wang, H., Jang, Y. I. & Huang, B. TEM study of electrochemical cycling-induced damage and disorder in LiCoO$_2$ cathodes for rechargeable lithium batteries. *J. Electrochem. Soc.* **146**, 473–480 (1999).
20. Watanabe, S., Kinoshita, M., Hosokawa, T., Morigaki, K. & Nakura, K. Capacity fade of LiAl$_y$Ni$_{1-x-y}$Co$_x$O$_2$ cathode for lithium-ion batteries during accelerated calendar and cycle life tests (surface analysis of LiAl$_y$Ni$_{1-x-y}$Co$_x$O$_2$ cathode after cycle tests in restricted depth of discharge ranges). *J. Power Sources* **258**, 210–217 (2014).
21. Gent, W. E. et al. Persistent state-of-charge heterogeneity in relaxed, partially charged Li$_{1-x}$Ni$_{1/3}$Co$_{1/3}$Mn$_{1/3}$O$_2$ secondary particles. *Adv. Mater.* **28**, 6631–6638 (2016).
22. Gabrisch, H., Yazami, R. & Fultz, B. The character of dislocations in LiCoO. *Electrochem. Solid-State Lett.* **5**, A111 (2002).
23. Huang, J. Y. et al. In situ observation of the electrochemical lithiation of a single SnO$_2$ nanowire electrode. *Science* **330**, 1515–1520 (2010).
24. Ulvestad, A. et al. Topological defect dynamics in operando battery nanoparticles. *Science* **348**, 1344–1347 (2015).
25. Yan, P. et al. Intragranular cracking as a critical barrier for high-voltage usage of layer-structured cathode for lithium-ion batteries. *Nat. Commun.* **8**, 14101 (2017).
26. Pfeifer, M. A., Williams, G. J., Vartanyants, I. A., Harder, R. & Robinson, I. K. Three-dimensional mapping of a deformation field inside a nanocrystal. *Nature* **442**, 63–66 (2006).
27. Clark, J. N. et al. Three-dimensional imaging of dislocation propagation during crystal growth and dissolution. *Nat. Mater.* **14**, 780–784 (2015).
28. Takahashi, Y. et al. Bragg X-ray ptychography of a silicon crystal: Visualization of the dislocation strain field and the production of a vortex beam. *Phys. Rev. B* **87**, 121201 (2013).
29. Nye, J. F. & Berry, M. V. Dislocations in wave trains. *Proc. R. Soc. A* **336**, 165–190 (1974).
30. Hull, D. & Bacon, D. J. *Introduction to Dislocations* 5th edn. (Elsevier, Oxford, 2011).
31. Qi, Y., Hector, L. G., James, C. & Kim, K. J. Lithium concentration dependent elastic properties of battery electrode materials from first principles calculations. *J. Electrochem. Soc.* **161**, F3010–F3018 (2014).
32. Yu, H. et al. Electrochemical kinetics of the 0.5Li$_2$MnO$_3$·0.5LiMn$_{0.42}$Ni$_{0.42}$Co$_{0.16}$ O$_2$ 'composite' layered cathode material for lithium-ion batteries. *RSC Adv.* **2**, 8797–8807 (2012).
33. Fell, C. R. et al. High pressure driven structural and electrochemical modifications in layered lithium transition metal intercalation oxides. *Energy Environ. Sci.* **5**, 6214–6224 (2012).
34. Qian, D., Xu, B., Chi, M. & Meng, Y. S. Uncovering the roles of oxygen vacancies in cation migration in lithium excess layered oxides. *Phys. Chem. Chem. Phys.* **16**, 14665–14668 (2014).

35. Delmas, C., Fouassier, C. & Hagenmuller, P. Structural classification and properties of the layered oxides. *Physica B + C* **99**, 81–85 (1980).
36. Poirer, J.-P. *Creep of Crystals* (Cambridge Univ. Press, Cambridge, 2005).
37. Sun, L., Marrocchelli, D. & Yildiz, B. Edge dislocation slows down oxide ion diffusion in doped CeO_2 by segregation of charged defects. *Nat. Commun.* **6**, 6294 (2015).
38. Szot, K., Speier, W., Bihlmayer, G. & Waser, R. Switching the electrical resistance of individual dislocations in single-crystalline $SrTiO_3$. *Nat. Mater.* **5**, 312–320 (2006).
39. Waser, R., Dittmann, R., Staikov, G. & Szot, K. Redox-based resistive switching memories - Nanoionic mechanisms, prospects, and challenges. *Adv. Mater.* **21**, 2632–2663 (2009).
40. Singer, A. et al. Nonequilibrium structural dynamics of nanoparticles in $LiNi_{1/2}Mn_{3/2}O_4$ cathode under operando conditions. *Nano Lett.* **14**, 5295–5300 (2014).
41. Elser, V. Phase retrieval by iterated projections. *J. Opt. Soc. Am. A* **20**, 40–55 (2003).
42. Luke, D. R. Relaxed averaged alternating reflections for diffraction imaging. *Inverse Probl.* **21**, 37–50 (2005).
43. Williamson, G. K. & Hall, W. H. X-ray line broadening from filed aluminium and wolfram. *Acta Metall.* **1**, 22–31 (1953).
44. Kresse, G. & Joubert, D. From ultrasoft pseudopotentials to the projector augmented-wave method. *Phys. Rev. B* **59**, 1758–1775 (1999).
45. Kresse, G. & Furthmüller, J. Efficiency of ab-initio total energy calculations for metals and semiconductors using a plane-wave basis set. *Comput. Mater. Sci.* **6**, 15–50 (1996).
46. Perdew, J. P. J., Burke, K. & Ernzerhof, M. Generalized gradient approximation made simple. *Phys. Rev. Lett.* **77**, 3865–3868 (1996).
47. Robertson, A. D. & Bruce, P. G. Mechanism of electrochemical activity in Li_2MnO_3. *Chem. Mater.* **15**, 1984–1992 (2003).

Author contributions

A.S., S.H., Y.S.M. and O.G.S. conceived the idea; A.S., S.H., D.C., C.F., A.U. and J.W. conducted the imaging experiments on LRLO nanoparticles, with assistance from E.M and R.H.; A.S. and N.H. performed the imaging experiments on NCA nanoparticles, with assistance from A.Z. and M.S.; S.H., C.F. and H.L. prepared the LRLO and NCA samples and performed the materials characterization and electrochemistry testing; A.S. analysed the imaging experiments with help from D.C. and O.G.S.; M.Z. performed the microstrain analysis with help from Y.S.M.; B.Q, Y.X. and Z.L. performed the superstructure restoration and subsequent electrochemistry testing; M.Z., T.W. and Y.S.M. performed the theoretical calculations; E.M. designed the sample environment. A.S. wrote the paper with input from all authors.

Competing interests

The authors declare no competing interests.

Additional information

Supplementary information is available for this paper at https://doi.org/10.1038/s41560-018-0184-2.

Reprints and permissions information is available at www.nature.com/reprints.

Correspondence and requests for materials should be addressed to Y.S.M. or O.G.S.

Publisher's note: Springer Nature remains neutral with regard to jurisdictional claims in published maps and institutional affiliations.